Adaptive Bidirectional Inductive Power and Data Transmission System

Jia-Jing Kao, Chun-Liang Lin, Yu-Chen Liu, Chih-Cheng Huang, and Hau-Shian Jian

***Abstract*—For the research of wireless power transfer, loosely coupled inductive power transfer (LCIPT) is one of the widely adopted technologies. There are already various researches focusing on development of high-efficiency LCIPT. However, when the transmission and receiver coils are misaligned, the power transfer efficiency will be significantly dropped. This article considers the change of mutual inductance when two induction coils are misaligned. A fuzzy control approach to solve for this problem by adaptively adjusting operational frequency is introduced. Experiments show that it can reduce the power transferring efficiency drop by 11% when two conduction coils are misaligned up to 50 mm. This research also supports adaptive maximum power transfer using tracking mechanism. Before conducting power transmission, the system can choose G2V or V2G according to the vehicle battery capacity via handshaking communication without the need of radio frequency links. In addition, the phase shift pulsewidth modulation technique is proposed for simultaneous data transmission enabling binary quadrature amplitude modulation for digital signal transmission. Fast over current protection is incorporated for power transfer safety when current overload happens. The transmission frequency of this article is controlled to meet the frequency specified by *SAE TIR J2954*.**

***Index Terms*—Electric vehicle, fuzzy control, loosely coupled inductive power transfer (LCIPT), SAE TIR J2954, wireless power transfer.**

I. Introduction

THE current loosely coupled inductive power transfer (LCIPT) transfer system is an innovative technology used for electric vehicles that exchanges power between two electrical objects through electromagnetic induction. Power transfers from the primary side to the secondary side through air gap. It is a type of power transmission method that does not make contact with conduction materials during power transmission [1]. Compared with traditional metal contact charging methods, LCIPT is more convenient and safe in practice because it can release the environmental constraints and resolve the safety problems in traditional wired charging. In addition, the electrical equipment connection will increase its impedance with the number of uses, which greatly affects the safety and reliability of the power supply [2].

Because of the advantages brought by LCIPT, more and more researchers focus in the relevant research, such as high performance magnetic coupling design [3], [4], electromagnetic compatibility [5], power transmission drive control [6], the technology related to wireless in-vehicle charging is becoming available for connected car solutions, and its development and innovation continues. Therefore, the *SAE TIR J2954* wireless charging specification [7] adopted by the society of automotive engineers (SAE) in 2016 established guidelines for wireless charging transmission in the electric vehicle industry.

The LCIPT system has matured in static charging for electric vehicles; however, there are still unsolved issues worthy of further investigation [8]. When the system like [9] has thought of data transmission, they have to rely on extra radio frequency (RF) links. This, of course, will bring in additional costs and lead to electromagnetic interference problems. Although [10] has proposed a bidirectional inductive power transfer (IPT) system, it can only conduct bidirectional power transfer but there is a lack of the function for bidirectional data transmission. Furthermore, if a misalignment appears between transmitting and receiving coils, the primary side will not be able to supply power to the secondary side smoothly. After a long period of operation in this case, the system might be burned out [11]. The system considered in [12] can resolve the coil misalignment problem, but it cannot perform bidirectional power/data transmission, and the *SAE TIR J2954* standard was not actually considered. Although [13] has proposed a bidirectional IPT system with coil misalignment detection, it cannot perform bidirectional data transmission, and there is no clear data transmission volume.

In [14], we have proposed a primitive fuzzy logic-based approach to deal with the issue of coil misalignment without the optimization sense. Motivated by the need to completely overcome the problems depicted abovementioned, this research task proposes an adaptive bidirectional wireless power and data transmission system for electric vehicles. The system eliminates the need of extra RF transmission links for data communication by directly transferring data via magnetic field induced by the induction coils. Considering the situation of misalignment of two

Manuscript received August 14, 2020; revised October 20, 2020; accepted December 18, 2020. Date of publication December 30, 2020; date of current version March 5, 2021. This work was supported in part by Ministry of Science and Technology, Taiwan under Grant MOST 106-2221-E-005-001-MY2 and in part by the Innovation and Development Centre of Sustainable Agriculture (IDCSA) under the Higher Education Sprout Project, Ministry of Education, Taiwan. Recommended for publication by Associate Editor C. Fernandez. *(Corresponding author: Chun-Liang Lin.)*

Jia-Jing Kao, Chun-Liang Lin, Yu-Chen Liu, and Hau-Shian Jian are with the Department of Electrical Engineering, Innovation and Development Center of Sustainable Agriculture, National Chung Hsing University, Taichung 402, Taiwan (e-mail: kao19681968@yahoo.com.tw; chunlin@dragon.nchu.edu.tw; ycliu.n1118@msa.hinet.net; qoo69600@gmail.com).

Chih-Cheng Huang is with the National Space Organization, Hsinchu 30078, Taiwan (e-mail: erichuang2014@hotmail.com).

This article has supplementary material provided by the authors and color versions of one or more figures available at https://doi.org/10.1109/TPEL.2020.3047069.

Digital Object Identifier 10.1109/TPEL.2020.3047069

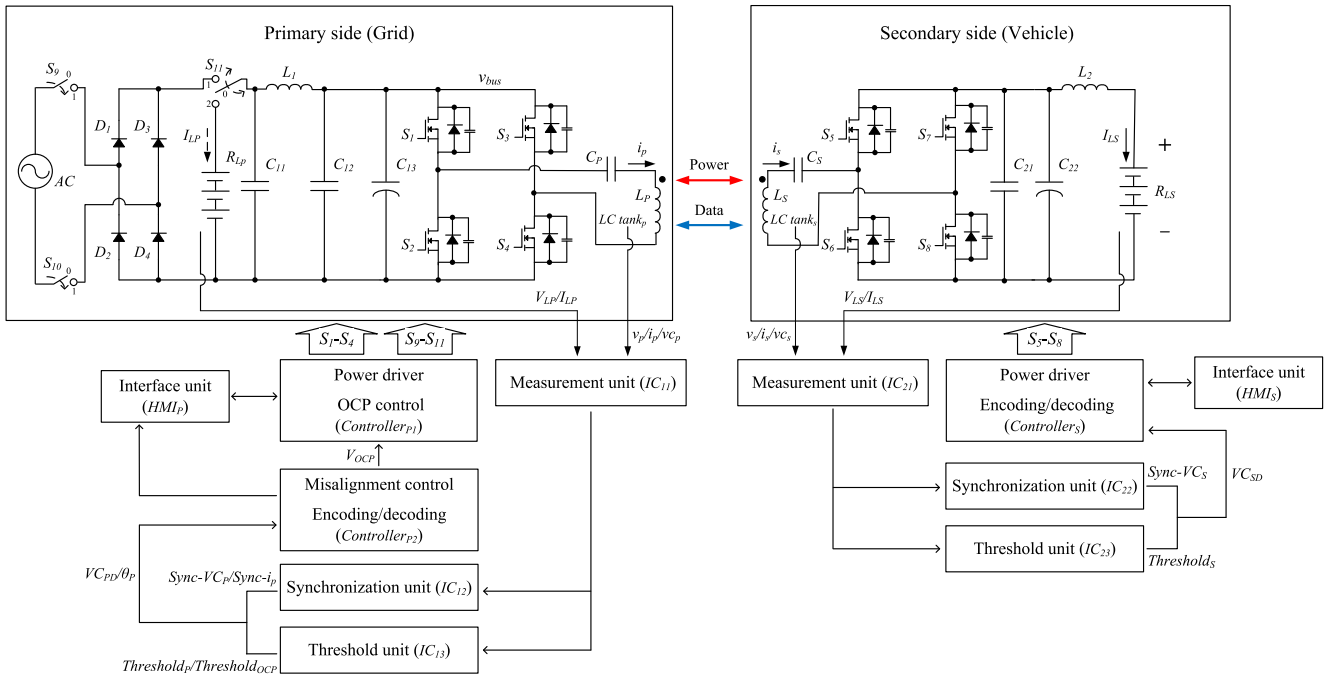

Fig. 1. Architecture of the proposed LCIPT system for electric vehicle charging.

coils, a fuzzy compensation scheme incorporated with the wireless power and data transmission system is proposed to adapt to the mutual inductance variation for the optimal power transfer. An efficient over current protection has also been incorporated. All of the ideas have been verified by real-word experiments.

The distinguished contributions of this research lie in three folds: first, establishing a bidirectional wireless power and data transmission scheme without additional wireless data transmission links; second, improving charging efficiency drop due to coil misalignment to optimize the power transfer performance by incorporating a fuzzy controller to accommodate for mutual inductance changes; and third, the system is protected by an advanced over current protection circuit to enable it coping with significant mutual inductance changes.

II. Inductive Power Transfer Architecture

A. Full Bridge Inverter

Fig. 1 shows the proposed architecture of a full bridge inverter. In which, the voltage $v_{\rm bus}$ is generated by a rectifier at the input, and the waveform signals represent the gate signals (V_{GS}) of S_1/S_4 and S_2/S_3, respectively. It is assumed that the pulsewidth modulation signal provided by each power switch is 50% of the on period (T_P), and a delay time ($T_{\rm Dead}$) is added simultaneously to the switching time of the inverter upper and lower arms. This is to prevent the two arms from being simultaneously turned ON at the switching instant and to ensure smooth operation at the zero voltage switching state (see Fig. 2).

The relationship between input and output is given by

$$v_p = \frac{4}{\pi} v_{\rm bus} \tag{1}$$

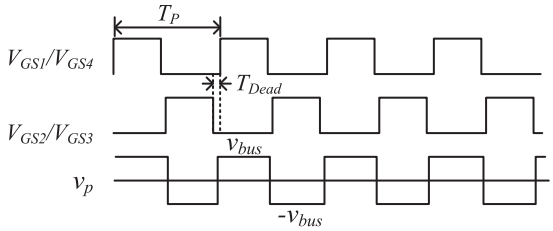

Fig. 2. Full bridge inverter signal waveforms.

TABLE I
Power Transferring Status

	Source	Load	S_9	S_{10}	S_{11}	S_1-S_4	S_5-S_8
G2V	Grid	R_{LS}	1	1	1	Inverter	Rectifier
V2G	Vehicle	R_{LP}	0	0	2	Rectifier	Inverter

where v_p represents the output voltage on the primary side and $v_{\rm bus}$ represents the input voltage.

B. Power Transfer

One can set the direction of power transmission through the interface unit (see Fig. 1). If the direction of power transmission is from the grid to the vehicle (i.e., G2V mode), S_1–S_4 constitute the inverter and S_5–S_8 constitute the rectifier. Table I shows the status of each device in both cases.

The driving mechanism is phase shifted PWM (PSPWM). First, the duty cycle of S_1–S_4 is fixed at 50%, S_3/S_4 are moved to generate a phase change, thereby changing the inverter output current. Figs. 3 and 4 show, respectively, the S_3/S_4 phase shifts

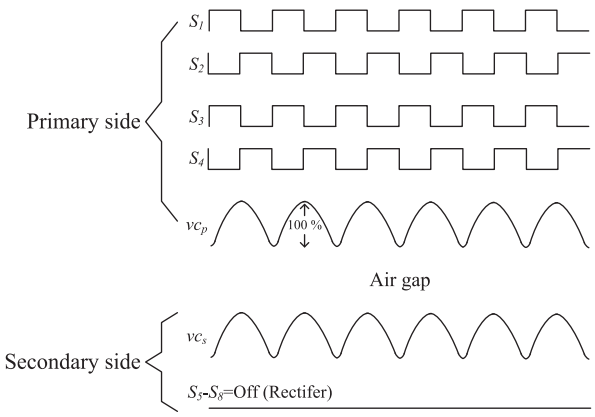

Fig. 3. S_3/S_4 phase shifts of 0 degrees (G2V 100%).

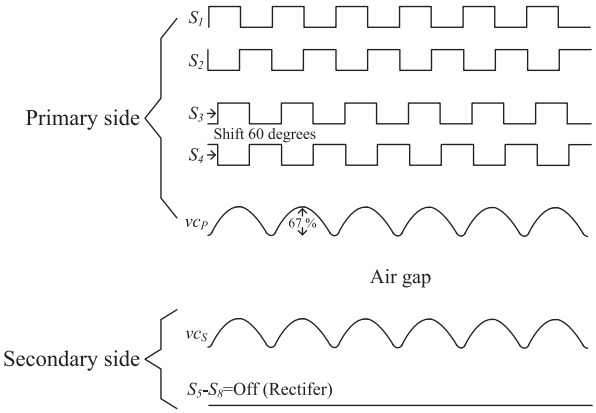

Fig. 4. $S_3/S4$ phase shifts of 60 degrees (G2V 67%).

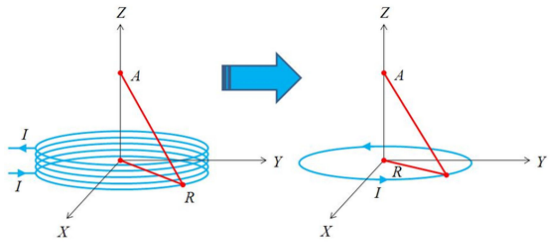

Fig. 5. Magnetic field strength generated by coil current on the metal wire.

of 0° (100%) and 60° (67%) and voltage change of the compensation capacitor C_P on the primary side (T_{Dead} not shown for sake of briefness).

C. Induction Coil Coupling Principle

Fig. 5 shows the three-dimensional magnetic field strength generated by the current in the metal wire. The magnetic field strength H at the center point above the ring wire can be expressed by

$$H = \frac{IR^2}{\sqrt[2]{(R^2+z^2)^3}} \tag{2}$$

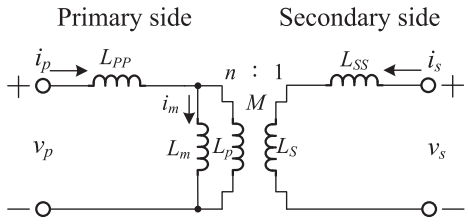

Fig. 6. Equivalent circuit of the noncontact inductive coupling coils.

where R is radius of the coil and I is coil current. Therefore, the larger the radius of the coil, the better the sensitivity to the vertical distance. If R is smaller, sensitivity to the vertical distance is relatively decreasing.

Fig. 6 illustrates the equivalent circuit model of the noncontact inductive coupling coils, where v_p and v_s are the primary side and secondary side voltages, respectively, i_p and i_s are the currents on both sides, L_P and L_S are the inductances on the respective side, M is the mutual inductance. L_{PP} and L_{SS} are, respectively, the primary and secondary side leakage inductances, L_m is the magnetizing inductance, I_m is the magnetizing current, and n is the coil turn ratio between the primary and secondary sides.

When converting it into an ideal coil equivalent circuit, the following relationship can be obtained:

$$L_m = nM \tag{3}$$

$$L_{PP} = L_P - nM \tag{4}$$

$$L_{SS} = L_S - \frac{M}{n}. \tag{5}$$

The equivalent inductance value L_{PS} seen from the primary side is given by

$$L_{PS} = L_P - \frac{M^2}{L_S}. \tag{6}$$

Bring this into the coupling coefficient K given by

$$K = \frac{M}{\sqrt{L_P L_S}} \tag{7}$$

yields

$$K = \sqrt{1 - \frac{L_{PS}}{L_P}}. \tag{8}$$

Obviously, reducing the magnetic flux leakage increases the coupling coefficient.

D. Resonance Compensation Circuit Principle

Since reactance of the capacitor and the inductor has a phase difference of 180°, the reactance will cancel each other under certain condition and frequency [15]. In the LCIPT system, the coil is loosely coupled and has a large leakage inductance, which reduces efficiency of power transmission. A common way to improve the leakage inductance is to add a compensation capacitor to the circuit on both sides of the system, thereby forming an inductance capacitance (LC) resonant circuit, and effectively eliminating parasitic parameters of some components in the circuit.

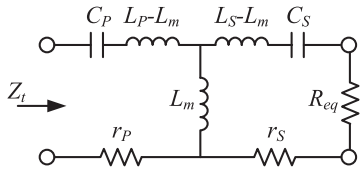

Fig. 7. Equivalent circuit of the *S-S* architecture.

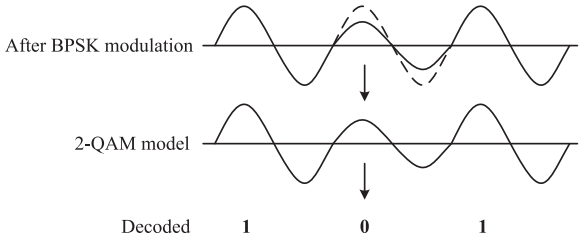

Fig. 8. Signal modulated and decoded waveforms (G2V mode).

Fig. 7 shows the equivalent impedance circuit of the series-series (*S-S*) architecture which we adopt. In which, L_m is the mutual inductance between induction coils of the primary and secondary sides, R_{eq} is the equivalent load resistance, and Z_t is the total impedance obtained for this architecture. It can be seen from

$$P_L = \left(\frac{v_{in}}{Z_t}\right)^2 R_{eq} \tag{9}$$

where the power transferred to the load, P_L, will reach its maximum when Z_t is minimized. Therefore, Z_t plays a key role in the wireless power transmission.

When designing an LC resonant circuit, its power factor (PF) must be considered. It is well-known that if $\mathrm{PF} = 1$, the power generated by the system can be consumed by the load leading to the most effective output [16].

III. Communication Architecture and Protocol

A full bridge inverter is considered, which uses PSPWM to simulate binary phase shift keying (BPSK) signals to achieve 2-QAM digital signals for data transmission (G2V mode). There are several digital signal modulation techniques such as amplitude shift keying, phase shift keying, frequency shift keying, and quadrature amplitude modulation (QAM). The BPSK digital signal module is constructed here with the modulated signals of "1" and "0" denoted, respectively, by

$$S_0(t) = \sqrt{\frac{2E_b}{T_b}} \cos\left(2\pi f t + \frac{\pi}{3}\right), 0 \le t \le T_b \tag{10}$$

$$S_1(t) = \sqrt{\frac{2E_b}{T_b}} \cos\left(2\pi f t\right), 0 \le t \le T_b \tag{11}$$

where f is the carrier signal, E_b and T_b are, respectively, the transmission energy and transmission time per bit.

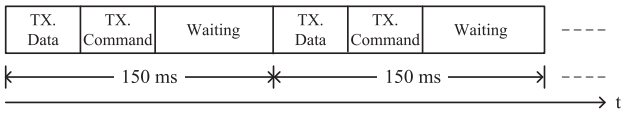

Fig. 9. Communication protocol.

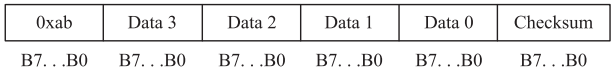

Fig. 10. Data and command packet transmission.

Fig. 8 shows the 2-QAM model generated after BPSK modulation. The process is used to achieve the purpose of simultaneous power and data transmission. The communication protocol here adopts the one-wire protocol [17].

Interface unit of the secondary side (HMI_S) transmits the measured voltage (V_{LS}) and current (I_{LS}) to the primary side (150 ms) through the modulation of S_6/S_8. Its data format might include vehicle number, voltage, current, and any warning messages. The interface unit on the primary side (HMI_P) uses modulation of S_1–S_4 to send commands to the secondary side. To avoid collision of feedback data and modulated command, the communication sequence is defined as in Fig. 9. Fig. 10 illustrates schematic diagram of data and command packet transmission. When the secondary side controller ($Controller_S$) feedbacks a data packet, the primary side controller ($Controller_{P1}$) chooses whether to send a command packet.

A. Bidirectional Signal Modulation

The system is designed to mutually transmit power, data and commands on both sides via the alternating magnetic field in LC tank. Fig. 11 demonstrates transmission of the data (0×96) from the secondary side to the primary side. When the system conducts data transmission, $Controller_S$ modulates S_6/S_8 and sends serial data bits "0" and "1", it then synchronizes the *Sync-VC*$_S$ signal. When the modulated bit is "0", S_6/S_8 is "1", and their instantaneous power will be temporarily stored in the *LC tank*$_S$; this will cause vc_p of the primary side to drop. $Controller_{P2}$ decides that the bit "0" is within the time interval T (*Sync-VC*$_P$ period), and $vpkc_p$ is less than $Threshold_P$, which means T_P (0); otherwise, it is T_P (1).

We set the level of $Threshold_P$ as follows

$$Threshold_P = \frac{vpkc_p(0) + vpkc_p(1)}{2} \tag{12}$$

where $vpkc_p(0)$ and $vpkc_p(1)$ are the primary side vc_p peak voltage levels referred, respectively, to the digits "0" and "1".

The transmitted command on the primary side is controlled by $Controller_{P1}$ that can change output voltage of the inverter of the primary side (see Fig. 12). In the figure, when the bit "0" is adjusted, vc_p output voltage will decrease from 100% to 67%; this will cause vc_s on the secondary side to decrease. $Controller_S$ decision bit "0" is within the time T (*Sync-VC*$_S$ period). When $vpkc_s$ is less than $Threshold_S$, it represents T_S (0); otherwise, it is T_s (1).

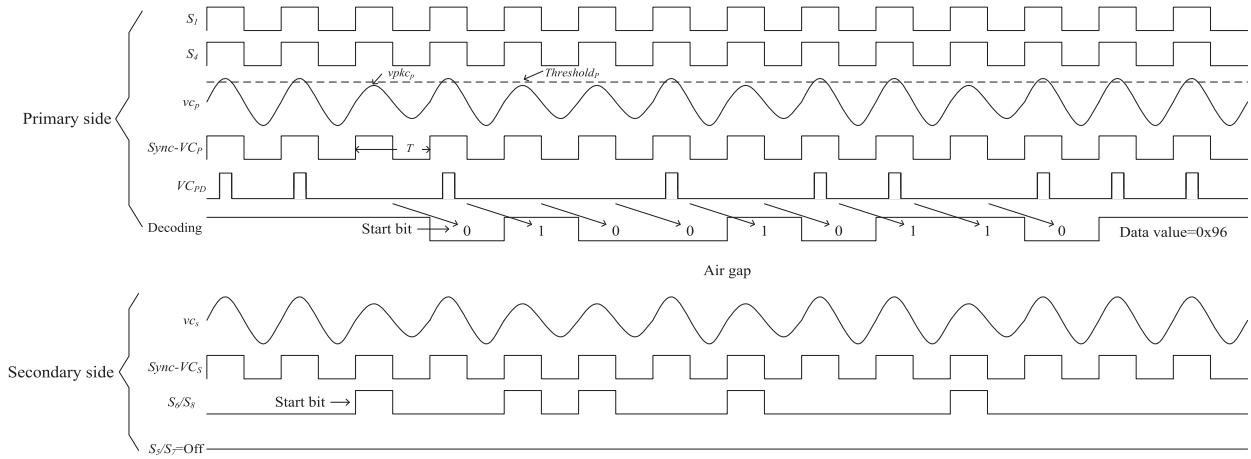

Fig. 11. Power transfer of the G2V mode and data feedback.

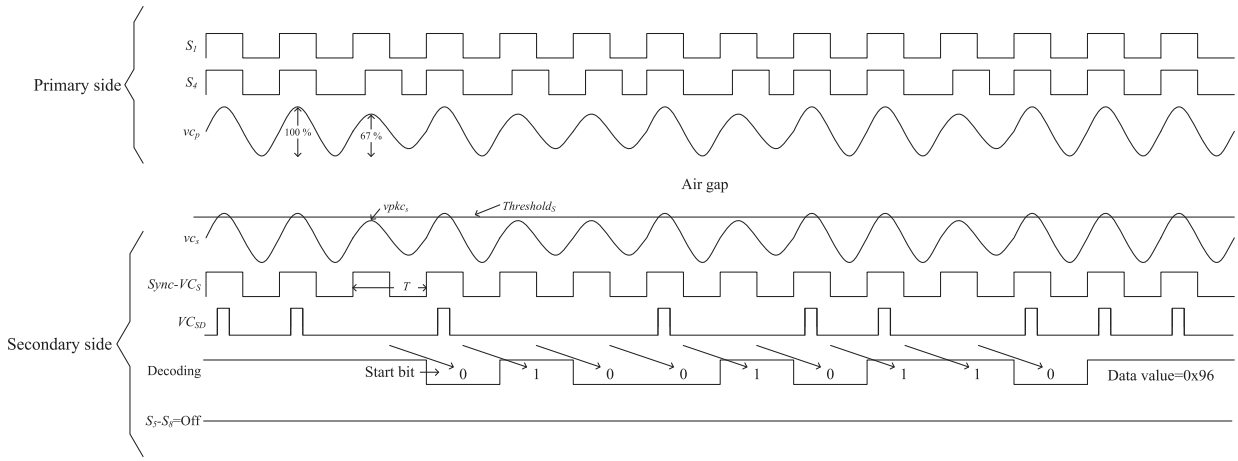

Fig. 12. Power and command transferring scheme for the G2V mode.

We set the $Threshold_S$ as follows

$$Threshold_S = \frac{vpkc_s(0) + vpkc_s(1)}{2} \tag{13}$$

where $vpkc_s(0)$ and $vpkc_s(1)$ are the secondary side vc_s peak voltage levels, referred, respectively, to the digits "0" and "1".

B. Handshaking Communication Before Power Transfer

Before conducting power transfer, both L_P and L_S need to be aligned within the permissible range. The power and data transfer works in two stages: first, the primary unit acquires battery status from the secondary unit via handshaking communication. The system runs for G2V or V2G in the next stage depending on the battery status. When the secondary unit responds message, which indicates insufficient battery capacity, the system will run the G2V mode. Otherwise, it will run the V2G mode. The roles of S_1–S_8 are listed in Table I. The handshaking communication protocol is listed in Table II.

Each handshaking communication package includes Handshaking $_{G2V}$ and $_{V2G}$ that utilizes the resonance principle [18] to transmit and receive commands and data.

TABLE II
HANDSHAKING COMMUNICATION PROTOCOL

Command	Data	Description
0100	1110	Secondary unit ready and Insufficient battery
	1100	Secondary unit ready and sufficient battery
	1111	Secondary unit faults and stop power transfer
1001	1000	Direction of power flow is G2V using efficient power transfer
1011		Direction of power flow is G2V using the adaptive maximum power
1101	1000	Direction of power flow is V2G using the efficient power transfer
1111		Direction of power flow is V2G using the adaptive maximum power

The resonant principle is shown in Fig. 13. In Fig. 13(a), the alternating current (i_1) shows a slow decay and produces longer free resonant time by resistance. Fig. 13(b) shows that i_1 is absorbed by the load (R_L), which yields shorter free resonant time. We utilize resonant time to detect load presentation and data transfer before fulfilling power transfer.

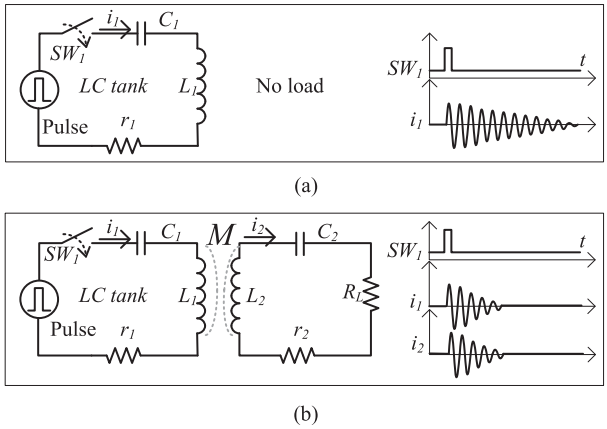

Fig. 13. Graphical explanation of the resonant principle. (a) Free resonant current by unit pulse injection to the LC tank. (b) Free resonant current to load via mutual inductance.

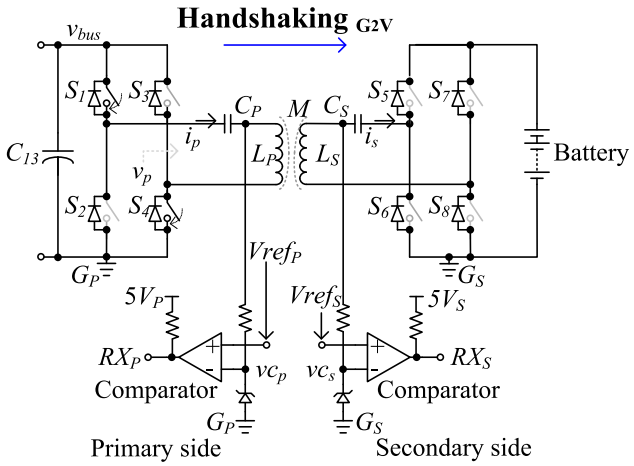

Fig. 14. Transceiver configuration of the handshaking $_{\mathrm{G2V}}$.

The configuration and handshaking communication of Handshaking $_{G2V}$ are shown in Fig. 14 with corresponding timing diagram illustrated in Fig. 15. In Fig. 14, the primary controller turns ON switches S_1 and S_4 to generate the starting bit or digit "0" and turns OFF S_1 and S_4 to generate "1" during T to send command to the secondary unit via the *S-S* architecture. The primary unit receives feedback digital bits via RX_P. In Fig. 15, the primary unit sends command "0b0100" and the secondary receives this command via RX_S. The primary processor diagnoses the suitable air gap by sensing $t_{\mathrm{free\_resonate}}$ in RX_P after receiving the starting bit. For example, if there is a suitable air gap between L_P and L_S, then $t_{\mathrm{free\_resonate}} << T$ since the load at the secondary side has absorbed energy in the LC tank of the primary unit through the air gap. On the other hand, $t_{\mathrm{free\_resonate}} > T$ means energy stayed within the LC tank of the primary side. The system will then halt power transfer.

The configuration and handshaking communication of Handshaking $_{V2G}$ are shown in Figs. 16 and 17, respectively. In Fig. 16, the secondary controller turns ON the switches S_5 and S_8 to generate the starting bit or digit "0" and turns OFF S_5 and S_8

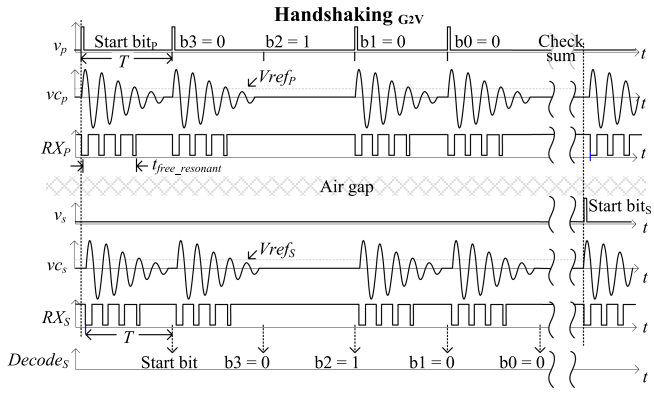

Fig. 15. Timing diagram of the handshaking $_{\mathrm{G2V}}$.

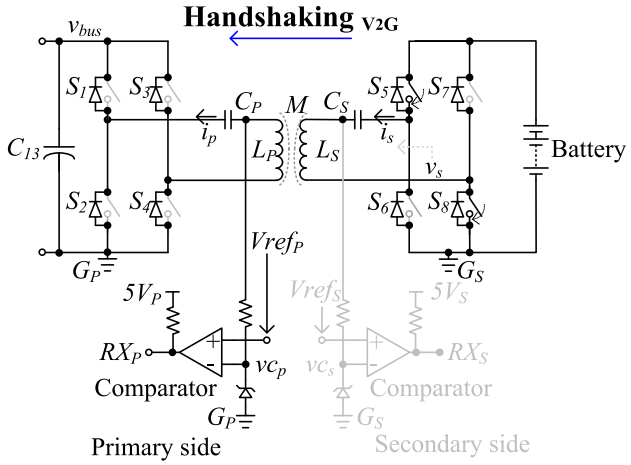

Fig. 16. Transceiver configuration of the handshaking $_{\mathrm{V2G}}$.

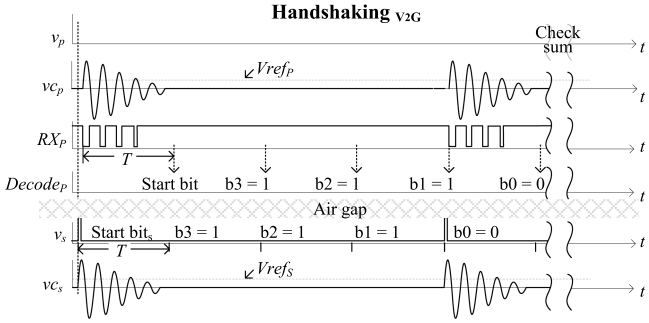

Fig. 17. Timing diagram of the handshaking $_{\mathrm{V2G}}$.

to generate "1" during T to send the primary unit. The secondary unit receives digital bits via RX_S. In Fig. 17, the secondary unit sends data "0b1110" and the primary unit receives the data via RX_P.

As demonstrated, the primary unit sends the command "0b0100" to acquire battery status at the secondary unit. The secondary unit responds "0b1110" answering insufficient battery capacity.

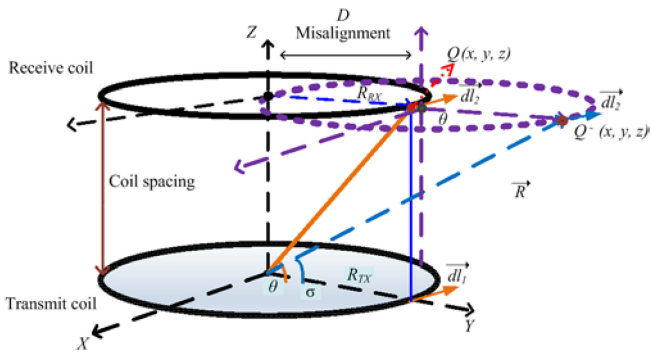

Fig. 18. Relative geometry of two conduction coils.

IV. Compensation for Mutual Inductance Change

Since the system operates in a noncontact environment, the physical contact between two conduction coils might change and shift during practical operations causing the system failed to operate at the optimum frequency. Compensation strategy is proposed to cope with this problem.

A. Model of Mutual Inductance

Fig. 18 shows the mathematical model of the coil position according to the well-known Biot–Savart law and Neumann formula in the case, where the transmission and receiving coils of the LCIPT system are aligned with each other.

The general formula given by

$$\frac{d\phi}{dt} = L_m \frac{dI}{dt} \tag{14}$$

where ϕ is the magnetic flux of the receiving coil, L_m is the mutual inductance, and I is the current flowing through the transmitting coil. Clearly, the current change rate of the transmitting coil is proportional to the change in the magnetic flux of the receiving coil.

Referring to Fig. 18, the magnetic flux density of the transmitting coil can be expressed as follows:

$$d\vec{B} = \frac{\mu_0 \times I\overrightarrow{dl_1} \times \vec{R}}{4\pi {R^3}_{TX}} \tag{15}$$

where, in the figure, Q is the assumed point on the receiving coil, $\overrightarrow{dl_1}$ and $\overrightarrow{dl_2}$ are the tangent between the two coils, R_{TX} and R_{RX} are the radii of the two coils, θ is the angle between the Q point and the origin projection, z is the air gap, D is the misaligned distance between two coil centers, and μ_0 is the magnetic permeability rate.

TABLE III
Simulation Settings

R_{eq} (Ω)	r_P (Ω)	r_S (Ω)	C_P (μF)	CS (μF)	L_P (μH)	LS (μH)	Gap (mm)
5.5	0.08	0.07	0.063	0.063	57.7	51.4	20

The magnetic flux density of the receiving coil is given by [19]

$$d\vec{B} = \frac{\mu_0 I R_{TX}}{4\pi} \int_0^{2\pi} \frac{R_{TX} - x\cos\theta}{\left(x^2 + z^2 + {R_{TX}}^2 - 2R_{TX}x\cos\theta\right)^{\frac{3}{2}}} d\theta \tag{16}$$

Equations (14)–(16) can be used to derive the mutual inductance

$$L_m = \frac{\mu_0}{4\pi} \int\int \frac{1}{R} dl_1 dl_2 \tag{17}$$

where R can be written as (18), shown at the bottom of this page.

When the induction coils are precisely misaligned, the transmission and reception components of $\overrightarrow{dl_1}$ and $\overrightarrow{dl_2}$ are related as

$$\overrightarrow{dl_1} \cdot \overrightarrow{dl_2} = R_{TX} R_{RX} \cos(\theta - \sigma)\, d\theta d\sigma \tag{19}$$

where σ is the angle formed by the receiving coil through the misalignment D.

Finally, bringing (18) and (19) into (17) gives the mutual inductance of the two coils in the misalignment [20]. It can be seen from the abovementioned derivations that when the two coils are aligned, the magnitude of the mutual inductance is independent of the current; however, if the air gap between two coils increases, the mutual inductance reduces accordingly.

B. S-S Type for Coil Misalignment

We simulate the mutual inductance change between the phase angle (θ) and the total impedance (Z_t) of the LCIPT system [14]. The frequency of the system is 83 kHz conformed to the *SAE TIR J2954* specification (81.3 to 90 kHz), and the compensation circuit architecture is *S-S* type. To make the simulation result close to the real-world situation, we first select the coils on the primary side and the secondary side of the system. Table III lists related parameters for use in the simulation.

Simulation results presented in Figs. 19 and 20 can be summarized as follows.

1) When the phase angle of the *S-S* type is negative, the mutual inductance changes stably, and the mutual inductance with the positive phase angle reacts symmetrically.
2) The total impedance will not change drastically due to mutual inductance changes.
3) The *S-S* type has the advantage for control, and the compensation strategy can be implemented easily on both of the transmitting/receiving sides.

$$R = \sqrt{{R_{TX}}^2 + {R_{RX}}^2 + z^2 + D^2 - 2R_{TX}R_{RX}\cos(\theta - \sigma) + 2R_{RX}D\cos\sigma - 2R_{TX}D\cos\theta} \tag{18}$$

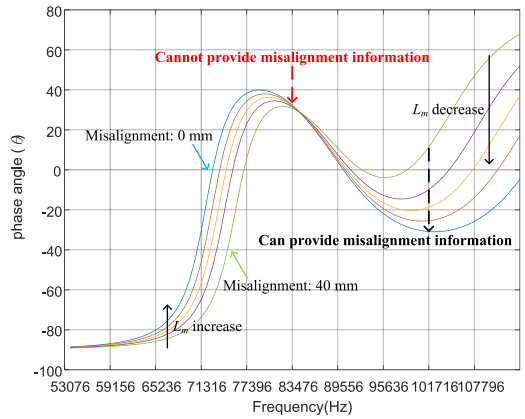

Fig. 19. Relationship between phase angle and mutual inductance under different coil misalignments (air gap fixed at 20 mm).

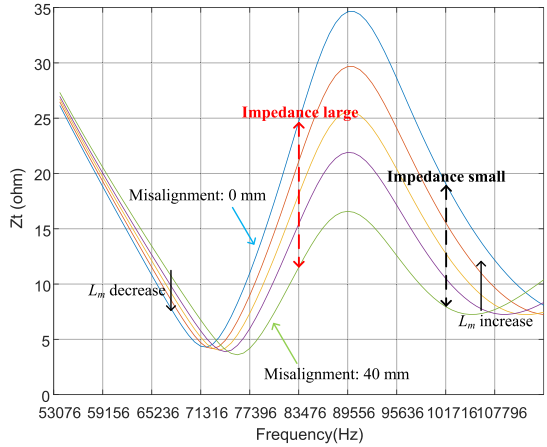

Fig. 20. Relationship between total impedance and mutual inductance under various induction coil misalignments (air gap fixed at 20 mm).

TABLE IV
RELATIONSHIP BETWEEN MISALIGNMENT AND COUPLING COEFFICIENT

Air gap: 20 mm					
Misalignment (mm)	0	10	20	30	40
L_m (μH)	25.15	23.25	21.55	19.9	17.2
K	0.46	0.43	0.4	0.36	0.32

Moreover, by taking the simulated mutual inductance value into (7) for calculation, the relationship between the mutual inductance and the coupling coefficient can be obtained. The result proves that as the air gap of the coil increases, the mutual inductance and coupling coefficient decrease (see Table IV). Therefore, we can summary the influence of misalignment or air gap on the mutual inductance of the system according to the operating conditions.

C. Compensation Under Coil Misalignment

As seen from Figs. 19 and 20, there is a close correlation between frequency, phase angle, coil misalignment, and total impedance from 70 to 100 kHz. Therefore, the phase angle and operating frequency detected by the primary side measurement unit (IC_{11}) can be used to adjust the optimal operating frequency of the system through the primary side controller ($Controller_{P2}$), thereby solving the problem of coil misalignment.

TABLE V
FUZZY INFERENCE RULE BASE

		Phase angle (θ)				
		NB	***NS***	***Z***	***PS***	***PB***
Frequency (f_n)	***NB***	*PB*	*PB*	*PB*	*PB*	*PS*
	NS	*PB*	*PS*	*PS*	*PS*	*PS*
	Z	*NS*	*NS*	*Z*	*Z*	*Z*
	PS	*NS*	*NS*	*NS*	*NS*	*NS*
	PB	*NB*	*NB*	*NB*	*NB*	*NB*

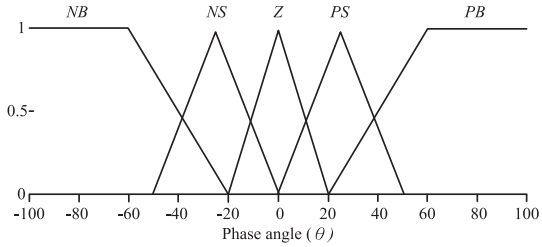

Fig. 21. Membership functions of the fuzzified phase angle.

Consider the system that meets the frequency of *SAE TIR J2954* with fuzzy control being used to achieve the optimal power transferring efficiency. Table V lists the established fuzzy rule base. It uses a typical trigonometric function to characterize the membership function because its calculation is relatively simple, fast, and easy to implement on the microcontroller for real-time control.

Based on the fuzzified input variables, we adjust the current frequency (f_n) and phase angle (θ) through fuzzy logic decision. Five fuzzy sets considered involve negative small (*NS*), negative large (*NB*), positive large (*PB*), positive small (*PS*) and zero (*Z*). The fuzzy inference rule adopted is the Mamdani method, and defuzzification is the center of gravity (CoG) method. For discrete triangular linear functions, the CoG method is obtained by moments of area defined by

$$\hat{y} = \frac{\sum_{y_i} y_i \mu(y_i)}{\sum_{y_i} \mu(y_i)} \tag{20}$$

where $\hat{y}$ is the defuzzified value and $\mu(y_i)$ is the membership value of the corresponding value y_i projected on the x-axis.

Figs. 21 and 22 depict the proposed membership functions. Fig. 23 showing relationship among three factors, which enable the system to perform bidirectional power and data transmission under the proposed system architecture. Fig. 24 explains operational flow of fuzzy control for adaptation of the misaligned induction coils.

D. Adaptive Maximum Power Transfers

This system employs an *S-S* architecture to link the primary side and secondary side for power and data transfer (see Fig. 7).

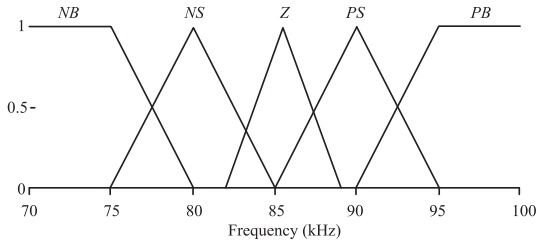

Fig. 22. Membership functions of the fuzzified frequency.

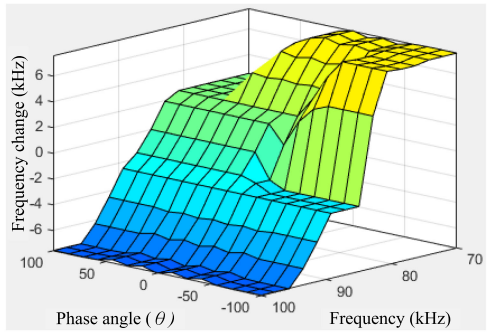

(a)

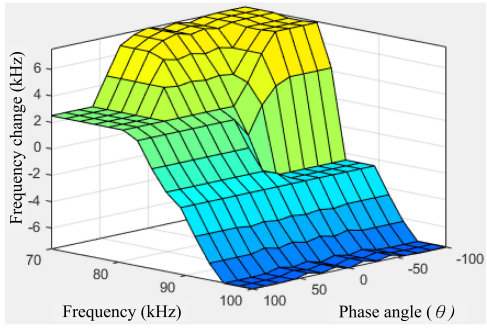

(b)

Fig. 23. Mapping of the two-input, one-output fuzzy controller. (a) Right view of the relationship between the three factors. (b) Left view of the relationship between the three factors.

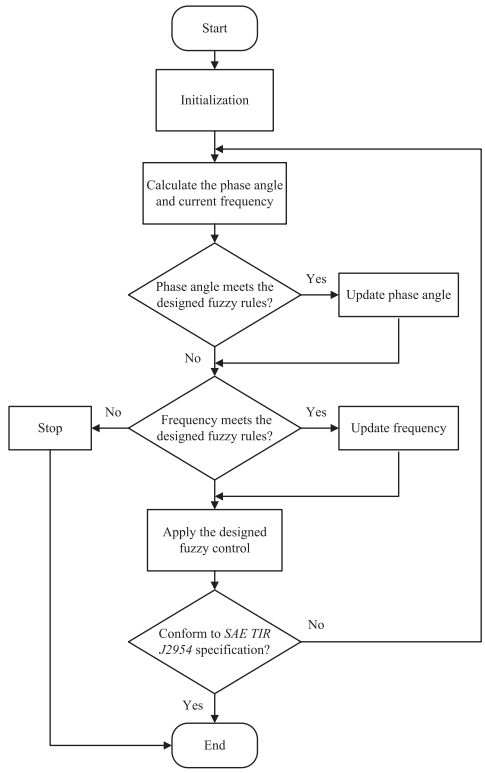

Fig. 24. Operational flow of fuzzy control when the induction coils are misaligned.

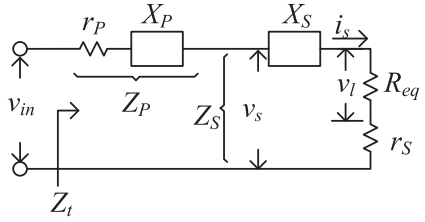

Fig. 25. Simplified representation of *S-S* architecture.

The simplified circuit of the *S-S* architecture is shown in Fig. 25. The total impedance Z_t (21) combines the real part and imaginary part (22) with the phase angle shown in (23). The power of load (P_L) is given by (24). If the air gap or misalignment varies between L_P and L_S, I_m will be affected and reflected in θ. If θ increases, P_L decreases accordingly as indicated by (24). Therefore, the system must increase i to keep P_L. However, increasing i will result in power consumption increased by r_P and r_S. Therefore, an efficient power transfer method is first proposed to keep θ by changing the operating frequency. When the system currently runs the G2V mode, the ON-OFF status of the switches S_1–S_4 is controlled by varying operating frequencies to generate the consistent frequency of the current injecting LC tank at the primary side, which will alter the total impedance Z_t accordingly since I_m is changed.

$$Z_t = (r_P + R_{eq} + r_S) + (X_P + X_S) \tag{21}$$

$$Z_t = Re + jI_m \tag{22}$$

$$\theta = \tan^{-1}(I_m/Re) \tag{23}$$

$$P_L = v_l i_S \cos\theta \tag{24}$$

An adaptive maximum power transfer is also proposed to reduce the charging time. We continuously adjust the operating frequency to alter Z_P being consistent with $Z_S{}^*$. The operational flow chart is illustrated in Fig. 26 and is explained as follows.

1) Initial parameters to be set including operating frequency (*OF*), delta frequency (*DF*), etc.
2) Wait for the main loop timing, such as 100 ms.
3) Calculate i_p, Z_P, Z_S, and Err_n.
4) Check if i_p is over the threshold. This limits i_p to avoid failure of S_1–S_8.

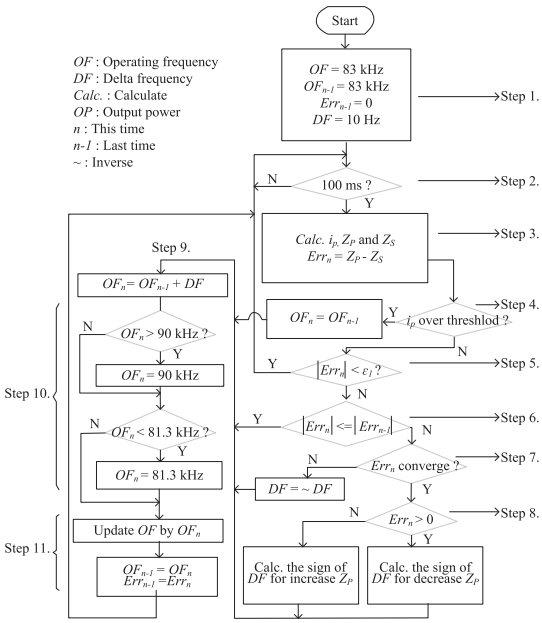

Fig. 26. Operational flowchart of the adaptive maximum power transfer.

5) Check if $|Err_n| \leq \varepsilon_1$ (ε_1 is a small positive constant). If yes, returns to step 2 to halt the iteration; otherwise, proceed to Step 6.
6) Check if $|Err_n|$ is less or equal to that of $|Err_{n-1}|$. If yes, goes to Step 9, otherwise proceeds to step 7.
7) Check if $|Err_n|$ has converged within a period of time. If no, it than inverses *DF* and moves on to step 9; otherwise, proceed to step 8.
8) Check if $Err_n > 0$. If yes, calculate the sign of *DF* using the measured value of v_{bus}, i_p, and θ to reduce Z_P after updating *OF*; otherwise, calculate the sign of *DF* using v_{bus}, i_p, and θ to increase Z_P after updating *OF*.
9) Update OF_n by adding *DF*.
10) OF_n limited within 81.3 kHz $\sim$ 90 kHz to comply with *SAE TIR J2954*.
11) Update $OF_{n\text{-}1}$ to OF_n, and update $|Err_{n-1}|$ by Err_n. Proceed to Step 2.

E. Over Current Protection

Typical OCP configuration is shown in Fig. 27(a), which involves primary controller, optoelectronic isolator, inverter, LC tank, over current detector, and measuring unit. The measuring unit calculates the load impendence. The current (i_p) phase is related to voltage (vc_p), which supports fuzzy control to generate efficient power transfer or adaptive maximal power transfer using the tracking method. The general over current detector monitors the levels of i_l and i_r when power transfer is operating. If either i_L or i_R is over the threshold level V_T, the over current signal (active low) go to $\overline{OC_1}$ or $\overline{OC_2}$ through an optoelectronic isolator. This will cutoff i_p by a propagation delay $\Delta\tau$ (from over current detected to turn OFF S_1–S_4). In general, $\Delta\tau$ costs 3–10 μs, which does not meet the current requirements in security.

To improve, an improved over current protection is proposed as shown in Fig. 27(b), which adds a shortcut to cutoff i_p by an

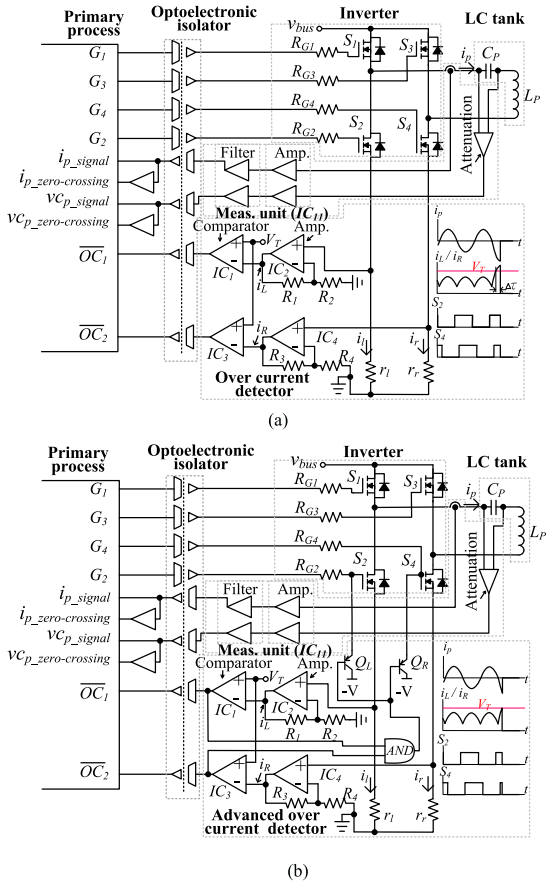

Fig. 27. Comparison of two over current protection designs. (a) Typical over current protection circuit. (b) Improved over current protection circuit.

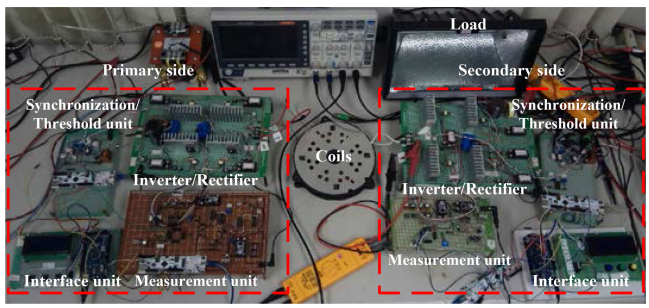

Fig. 28. Hardware architecture of the overall system.

AND gate realized by the transistors Q_L and Q_R. Once over current is detected, both of Q_L and Q_R will be activated to turn OFF S_2 and S_4 and cutoff i_p immediately. This significantly reduces $\Delta\tau$ while compared with that of the previous one.

V. Design and Integration

Critical components of the circuit include inverter /rectifier, measurement unit, synchronization/threshold unit, and interface. Fig. 28 displays hardware of the overall system for experiments.

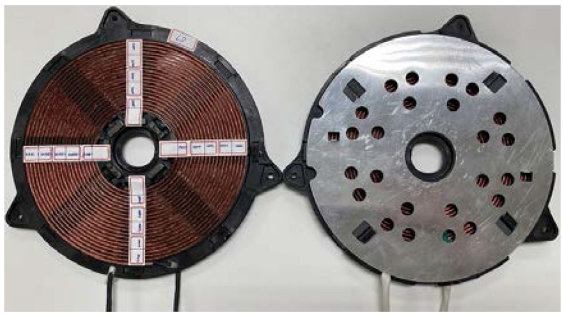

Fig. 29. Induction coil for transmitting power and data.

TABLE VI
LCIPT SYSTEM PARAMETERS

Operating frequency	83 kHz
Rated output power	800 W
Load resistance (R_{LS})	5.5 Ω
Primary side coil inductance (L_P)	57.7 μH
Primary side capacitance (C_P)	0.063 uF
Mutual inductance (L_m)	17.2 μH-25.15 μH
Secondary side coil inductance (L_S)	51.4 μH
Secondary side capacitance (C_S)	0.063 μF
Coil architecture	Spiral
Coil winding method	Open
Wire diameter	2.0 mm
Coil diameter	200 mm
Number of coil turns	23 turns
Nominal transmission distance (air gap)	20 mm

A. Realization of Controller

The microcontroller (*NUC505xx*) [21] is supported by an *ARM Cortex-M4* 32-bit core operated at 100 MHz. It is responsible for processing power drive, command modulation, and compensation for the coil misalignment. The MOSFETS used in the full bridge inverters on both sides are *C2M0080120D* [22].

B. Coil and Load

The induction coils on both sides of the system are symmetrical to each other. The structure is spiral and the winding method is open so that the two ends of the coil are not connected to each other (see Fig. 29). A 1.5-KW halogen lamp searchlight was used as the load. Table VI lists related parameters associated with the designed LCIPT system.

VI. EXPERIMENTAL VERIFICATION

A. Wireless Power Transfer

Fig. 30 shows the signal (command) waveforms of the LCIPT system working at 800 W output power in the G2V mode. Channels 1 to 4 show the voltage waveform of the compensation capacitor (C_P) on the primary side, the current waveform of the transmission coil (L_P) on the primary side, the voltage waveform of the compensation capacitor (C_S) on the secondary side, and the current waveform of the receiving coil (L_S) on the secondary side.

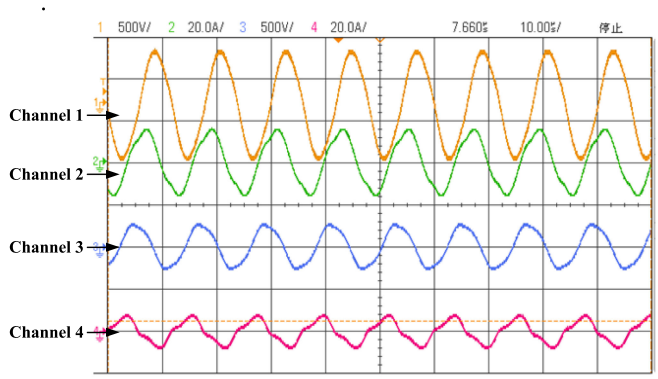

Fig. 30. LCIPT system worked at 800 W output power under the G2V mode.

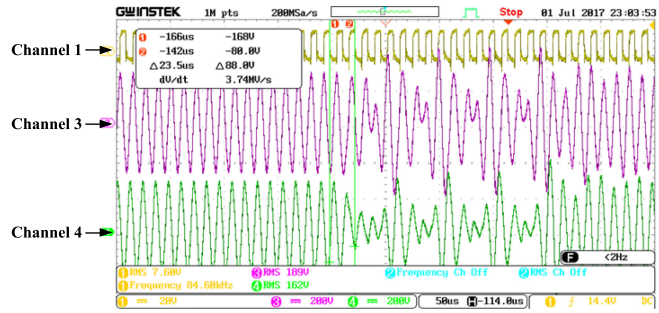

Fig. 31. Signal modulation on the secondary side.

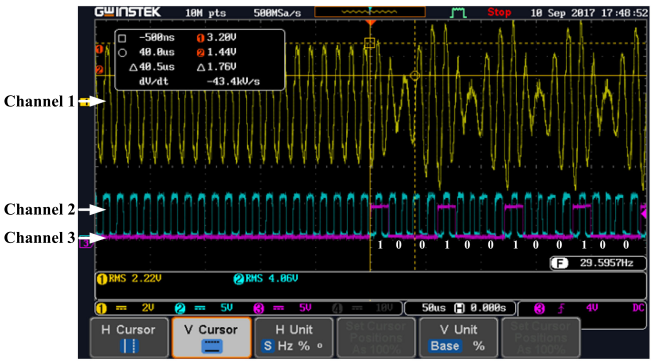

Fig. 32. Waveforms of data feedback.

B. Power Transfer From G2V and Data Feedback

Fig. 31 shows the waveforms of the secondary side signal modulation when the LCIPT is working at the G2V mode. Channel 1 shows the primary side PSPWM waveform, channel 3 shows the primary side LC tank voltage waveform, and channel 4 shows the secondary side LC tank voltage waveform. When there is voltage variation of the LC tank ($LC\ tank_S$) on the secondary side, voltage of the LC tank ($LC\ tank_P$) on the primary side will change accordingly according to the data feedback.

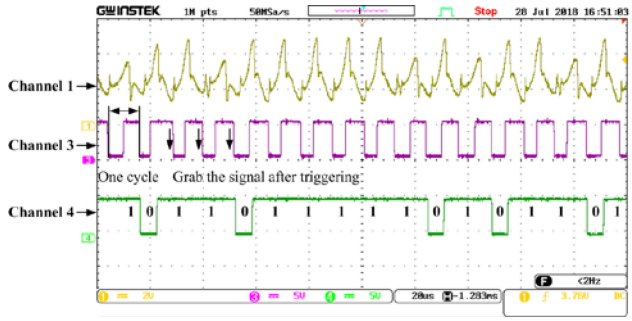

Fig. 33. Waveform diagram of signal modulation and decoding.

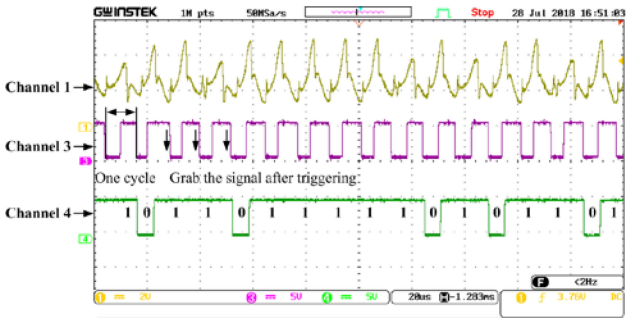

Fig. 34. Modulated and decoded waveforms for a serious of digitized data transfer.

Fig. 32 shows the waveforms of data feedback of the LCIPT system. Channels 1 to 3 show, respectively, the voltage waveform of the LC tank on the primary side, the zero crossing waveform of the primary side (*Sync-VC*$_P$), and the decoded waveform of the primary side (from *Controller*$_{P2}$). As shown, data feedback from the secondary side is decoded.

C. Power and Command Transfer From G2V

Fig. 33 displays waveforms of the signal modulation and data decoding scheme. Channel 2 shows the threshold set by data decoding requirement (*Threshold*$_S$). Channel 3 shows waveform change of the decoding circuit (VC_{SD}). Channel 4 shows the decoded digital waveform (from *Controller*$_S$). By refining circuit parameter settings, one would be able to distinguish the waveform difference of the signal modulation thereby distinguishing the difference between high and low levels.

Fig. 34 shows the modulated and decoded waveforms under different data transfer settings. Channel 1 shows the voltage waveform of the compensation capacitor (*VCs*) on the secondary side. Channel 3 shows the zero crossing waveform (*Sync-VC*$_S$). Channel 4 shows the decoded digital waveform (from *Controller*$_S$). In this case, the modulated data can still be successfully decoded.

To confirm the signal modulation will not affect the normal operation, we also examine the power transfer efficiency under different wattages. As seen from Fig. 35, the deviated power transfer efficiency can be remained within 4%.

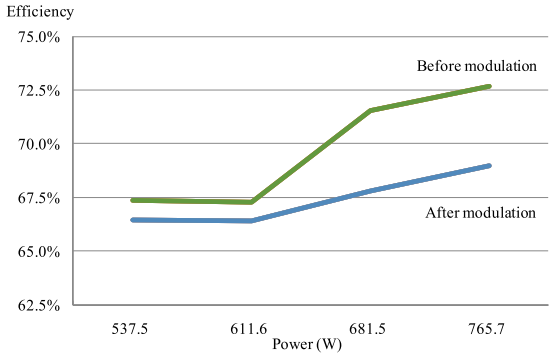

Fig. 35. Effect of signal modulation on the power transfer efficiency under different wattages.

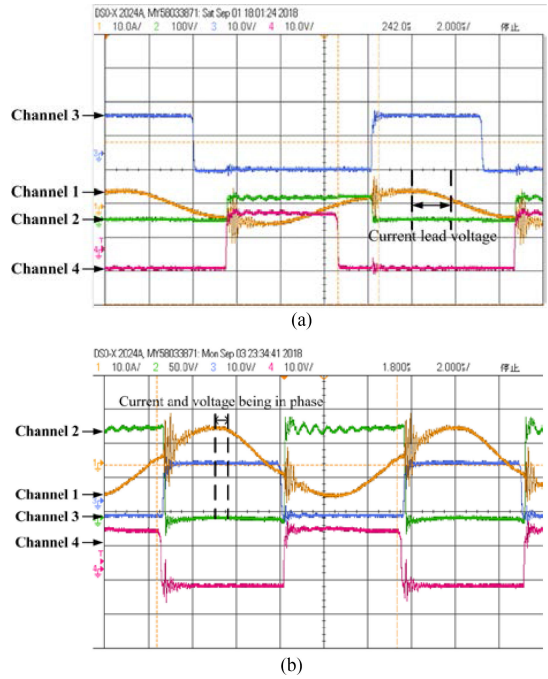

Fig. 36. Verification of the LCIPT system waveforms when induction coils are misaligned. (a) Waveforms of the LCIPT system when two induction coils are misaligned. (b) Waveforms of the LCIPT system when fuzzy control is adopted.

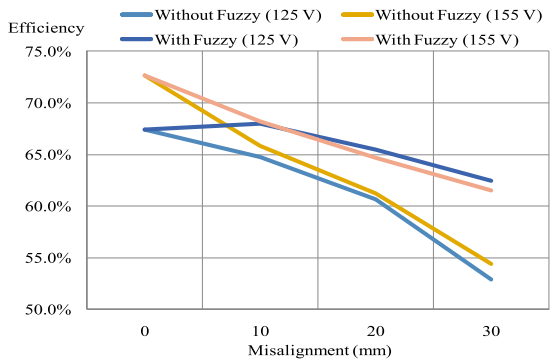

Fig. 37. Comparison of the power transferring efficiency under different voltage and coil misalignment.

Fig. 38. Trend of power transfer efficiency with respect to coil misalignment and control effectiveness.

D. Fuzzy Control of Coil Misalignment

When MOSFETs of the full bridge inverter are turned ON and OFF, the current flow through will exhibit a sine wave of positive and negative half cycles. If the two coils are misaligned, the current will be reversed ($\theta < 0$) leading to rapid arise of component temperature and affects system safety and reliability.

Fig. 36(a) shows the waveforms of the LCIPT system with coil misalignment (at 83 kHz). Channels 1 to 4 show, respectively, the primary side current waveform (i_p), the S_1 voltage waveform (V_{DS1}), and the gate waveforms of the primary side S_1/S_2 (V_{GS}). It can be found that when the coils are misaligned, i_p will significantly lead V_{DS1}. Fig. 36(b) shows the waveform under fuzzy control. It can be seen from the figure that the phase (θ_P) difference between i_p and V_{DS1} is significantly reduced.

We also tested the effect of fuzzy control to compensate for coil misalignment under different voltage levels and air gaps. It is apparent from Figs. 37 and 38 that the power transfer efficiency of the LCIPT system can be effectively improved by adjusting the current phase angle and system frequency. Especially, the improvement becomes significant when there is a significant coil misalignment. In addition, the proposed method shows significant effectiveness with various air gaps. Interested readers are invited to access the web link listed in [23] for real-world demonstration.

E. Over Current Protection

When the coils are misaligned or the load is short circuited, the input current on the primary side of the system arise accordingly. When it happened, the OCP intervenes to prevent the system from overloading. Fig. 39(a) shows the action of protection. In which, channels 1 to 4 show, respectively, the current waveform of the Hall sensor (i_p), the preset threshold ($Threshold_{OCP}$), the gate waveform of S_2 (V_{GS2}), and the waveform of cutting off S_2/S_4 (V_{OCP}). It can be seen from Fig. 39(b) that when the detected current exceeds the safety threshold, V_{GS2}/V_{GS4} is cutoff immediately which halts operation on the primary side accordingly.

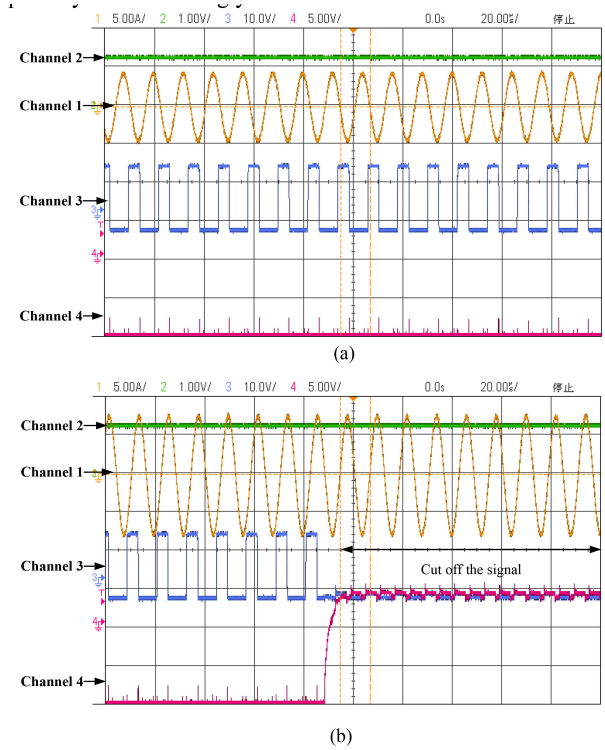

Fig. 39. Verification of the OCP function. (a) Before the OCP function activated. (b) After the OCP function activated.

F. Power Transmission Quality

This system employs an LC tank with *S-S* architecture, which can filter most of the harmonic elements when the switches are turned ON or OFF frequently. For example, the harmonic spectrum of the secondary current i_s, as shown in Fig. 40, whereas the output power is 800 W. There are significant frequency elements within three orders in the spectrum with $\mathrm{THD_F} = 23.08\%$. Since our primary unit has a low-pass filter constituted by L_1, C_{11}, C_{12}, and C_{13} shown as in Fig. 1. The arrangement will filter harmonic frequencies sent back to the grid. Moreover, our system employs

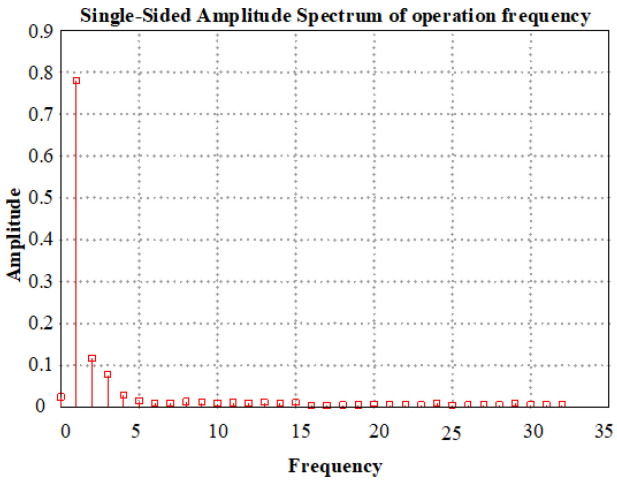

Fig. 40. Harmonic spectrum of current at the secondary side (worked at 83 kHz).

a load-detecting function in the handshaking communication stage to check load existence, which ensures energy will be fully transmitted to the secondary unit. Therefore, emission of high-order harmonics is considerably minimized.

VII. Conclusion

This article proposes an LCIPT system for electric vehicles with its architecture supporting simultaneous power and data transmission in both of the primary and secondary sides while accounting for mutual inductance changes with no extra RF links needed for data communication. The symmetrical circuit design allows the transmission and receiving sides to be adjusted as appropriate. Data transmission is fulfilled by BPSK to form 2-QAM which conforms to the one-wire protocol.

We have analyzed mutual inductance and total impedance between the induction coils to characterize correlation between the voltage and current phase angle while adjusting operating frequency to conform *SAE TIR J2954*. The proposed method can increase system efficiency more than 7.5% under high voltage and large conduction coil misalignment. Moreover, when the system operational status appears to be abnormal, a fast over current protection mechanism cutsoff gate commands within 4 μs to avoid the risk of damage to the inverter. Therefore, the integrated bidirectional wireless power and data transmission with coil misalignment compensation is considerably efficient with safety. The design presented is expected to be used for energy exchange between car batteries and apartment complex's energy storage tank, i.e., G2V and V2G.

The proposed design has met frequency requirements set by *SAE* standard; however, there are still rooms for further investigation such as vehicle charging integrity, induction coil design, electromagnetic interference, electromagnetic compatibility, and maximization of the power transferring efficiency. In addition, a refined fuzzy control rule base or an increase of the number of membership functions can be adopted to generate smoother current transition when the conduction coil deviation increases.

References

[1] D. J. Thrimawithana and U. K. Madawala, "A generalized steady-state model for bidirectional IPT systems," *IEEE Trans. Power Electron.*, vol. 28, no. 10, pp. 4681–4689, Oct. 2013.

[2] L. Chen, G. R. Nagendra, J. T. Boys, and G. A. Covic, "Double-coupled systems for IPT roadway applications," *IEEE Trans. Emerg. Sel. Top. Power Electron.*, vol. 3, no. 1, pp. 37–49, Mar. 2015.

[3] B. H. Choi, E. S. Lee, J. Huh, and C. T. Rim, "Lumped impedance transformers for compact and robust coupled magnetic resonance systems," *IEEE Trans. Power Electron.*, vol. 30, no. 11, pp. 6046–6056, Nov. 2015.

[4] C. Carretero, "Coupling power losses in inductive power transfer systems with litz-wire coils," *IEEE Trans. Ind. Informat.*, vol. 64, no. 6, pp. 4474–4482, Jun. 2017.

[5] G. B. Tait and R. E. Richardson, "Wireless channel modeling of multiply connected reverberant spaces: Application to electromagnetic compatibility assessment," *IEEE Trans. Electromagn. Compat.*, vol. 55, no. 6, pp. 1320–1327, Dec. 2013.

[6] J. M. Miller, O. C. Onar, and M. Chinthavali, "Primary-side power flow control of wireless power transfer for electric vehicle charging," *IEEE Trans. Emerg. Sel. Top. Power Electron.*, vol. 3, no. 1, pp. 147–162, Mar. 2015.

[7] Wireless power transfer for light-duty plug-in/electric vehicles and alignment methodology, J2954, 2019.

[8] T. D. P. Perera, D. N. K. Jayakody, S. K. Sharma, S. Chatzinotas, and J. Li, "Simultaneous wireless information and power transfer: Recent advances and future challenges," *IEEE Commun. Surv. Tut.*, vol. 20, no. 1, pp. 264–302, Dec. 2018.

[9] A. A. S. Mohamed, A. Meintz, P. Schrafel, and A. Calabro, "Testing and assessment of EMFs and touch currents from 25-kW IPT system for medium-duty EVs," *IEEE Trans. Veh. Technol.*, vol. 68, no. 8, pp. 7477–7487, Aug. 2019.

[10] L. Zhao, D. J. Thrimawithana, U. K. Madawal, and A. P. Hu, "A push–pull parallel resonant converter-based bidirectional IPT system," *IEEE Trans. Power Electron.*, vol. 35, no. 3, pp. 2659–2667, Mar. 2020.

[11] Y. Chen, B. Yang, Z. Kou, Z. He, G. Cao, and R. Mai, "Hybrid and reconfigurable IPT systems with high-misalignment tolerance for constant-current and constant-voltage battery charging," *IEEE Trans. Power Electron.*, vol. 33, no. 10, pp. 8259–8269, Oct. 2018.

[12] A. Babu and B. George, "Sensor system to aid the vehicle alignment for inductive EV chargers," *IEEE Trans. Ind. Electron.*, vol. 66, no. 9, pp. 7338–7346, Sep. 2019.

[13] Y. Liu, U. K. Madawala, R. Mai, and Z. He, "Primary-side parameter estimation method for bidirectional inductive power transfer systems," *IEEE Trans. Power Electron.*, vol. 36, no. 1, pp. 68–72, Jan. 2021.

[14] H. S. Jian, J. J. Kao, and C. L. Lin, "Adaptive wireless power charging system," in *Proc. IEEE Conf. Ind. Electron. Appl.*, May/Jun. 2018, pp. 627–632.

[15] Z. Yan, Y. Li, C. Zhang, and Q. Yang, "Influence factors analysis and improvement method on efficiency of wireless power transfer via coupled magnetic resonance," *IEEE Trans. Magn.*, vol. 50, no. 4, Apr. 2014, Art. no. 4004204.

[16] S. W. Lee and H. L. Do, "Soft-switching two-switch resonant AC–DC converter with high power factor," *IEEE Trans. Ind. Electron.*, vol. 63, no. 4, pp. 2083–2091, Apr. 2016.

[17] M. E. Cambronero, H. Macià, V. Valero, and L. O. Barbosa, "Modeling and analysis of the 1-wire communication protocol using timed colored petri nets," *IEEE Access*, vol. 6, pp. 27356–27372, May 2018.

[18] D. W. Hart, *Resonant Converters, Power Electronics*. New York, NY, USA: McGraw-Hill, 2010, ch. 9, pp. 387–427.

[19] Y. Cheng and Y. Shu, "A new analytical calculation of the mutual inductance of the coaxial spiral rectangular coils," *IEEE Trans. Magn.*, vol. 50, no. 4, Apr. 2014, Art. no. 7026806.

[20] Z. Luo and X. Wei, "Analysis of square and circular planar spiral coils in wireless power transfer system for electric vehicles," *IEEE Trans. Ind. Electron.*, vol. 65, no. 1, pp. 331–341, Jan. 2018.

[21] Nuvoton, Hsinchu, TWN, Microcontroller Products. 2015. [Online]. Available: https://direct.nuvoton.com/en/nuc505dl13y, Accessed on: May 20, 2019.

[22] Wolfspeed, Durham, NC, USA, Power Products. 2013. [Online]. Available: https://www.wolfspeed.com/c2m0080120d, Accessed on: Jun. 26, 2019.

[23] NCHU, Taichung, TWN, Research Contribution. 2020. [Online]. Available: https://youtu.be/fbmzE8y8t6s, Accessed on: Jul. 7, 2020.